Journal of Materials Science & Technology 54 (2020) 58–68

Contents lists available at ScienceDirect

Journal of Materials Science & Technology

journal homepage: www.jmst.org

Research Article

Microscopic stresses in carbon nanotube reinforced aluminum matrix composites determined by in-situ neutron diffraction

X.X. Zhang[a], J.F. Zhang[a], Z.Y. Liu[a], W.M. Gan[b], M. Hofmann[c], H. Andrä[d], B.L. Xiao[a,*], Z.Y. Ma[a,*]

[a] Shenyang National Laboratory for Materials Science, Institute of Metal Research, Chinese Academy of Sciences, Shenyang 110016, China
[b] German Engineering Materials Science Centre at MLZ, Helmholtz-Zentrum Geesthacht, D-85747 Garching, Germany
[c] Heinz Maier-Leibnitz Zentrum (MLZ), Technische Universität München, D-85747 Garching, Germany
[d] Fraunhofer Institute for Industrial Mathematics, Fraunhofer-Platz 1, Kaiserslautern 67663, Germany

ARTICLE INFO

Article history:
Received 25 November 2019
Received in revised form
23 December 2019
Accepted 28 January 2020
Available online 16 May 2020

Keywords:
Carbon nanotubes
Aluminum matrix composites
In-situ neutron diffraction
Load partitioning

ABSTRACT

One of the most desired strengthening mechanisms in the carbon nanotube reinforced aluminum matrix composites (CNT/Al) composites is the load transfer strengthening mechanism (LTSM). However, a fundamental issue concerning the LTSM is that quantitative measurements of load partitioning in these composites during loading are very limited. In this study, in-situ neutron diffraction study on the tensile deformation of the 3 vol.% CNT/2009Al composite and the unreinforced 2009Al alloy was conducted. The {311} and {220} diffraction elastic constants (DECs) of the 2009Al alloy were determined. Using those DECs the average stress in the 2009Al matrix of the composite was calculated. Then the average stress in the CNTs was separated by using the stress equilibrium condition. Computational homogenization models were also applied to explain the stress evolution in each phase. Predicted results agree with experimental data. In the present case, the average stress in the CNTs reaches 1630 MPa at the yield strength of the composite based on linear regression of the measured data, which leads to an increment of yield strength by about 37 MPa. As the result of this work, an approach to quantify load partitioning in the CNTs is developed for the CNT/Al composites, which can be applied to optimize the mechanical properties of the composites.

1. Introduction

Carbon nanotubes (CNTs), due to their superior mechanical properties, low density and good physical properties, are considered to be an ideal reinforcement for metal matrix composites (MMCs). CNTs reinforced aluminum (CNT/Al) composites are considered to be good candidate materials for widespread engineering applications, because of their excellent mechanical properties, good plastic formability and machinability [1–4].

A thorough understanding of the strengthening mechanisms at microscale is important for optimizing the mechanical properties of the CNT/Al composites, as well as the manufacturing process. George et al. [5] pointed out that three strengthening mechanisms exist in the CNT/pure-Al composites, which are thermal mismatch, Orowan looping and load transfer. Chen et al. [6] verified the existence of load transfer strengthening mechanism (LTSM) via in-situ tensile test of a CNT/pure-Al composite based on field emission scanning electron microscopy (SEM) technique. Later, Zhou et al. [7] also proved the existence of LTSM [7]. The shear strength of CNT/pure-Al interface was found to be about 24.8 MPa [7]. Besides the above mechanisms, grain refinement also caused significant strengthening effect in the CNT/Al composites [2,8–11].

Among all the potential strengthening mechanisms, the LTSM is the most desired one because it increases both the stiffness and the strength of the composites [12,13]. Meanwhile, the superior mechanical properties of the CNTs can only be utilized via the LTSM. However, the LTSM is not well understood yet. One fundamental issue of the LTSM is that quantitative measurements of load partitioning in these composites during loading are very limited [14].

In-situ synchrotron X-ray diffraction and neutron diffraction are novel experimental methods to analyze phase specific strains or stresses in engineering materials. These methods have been applied to investigate phase specific load partitioning in multi-phase mate-

* Corresponding authors.
E-mail addresses: blxiao@imr.ac.cn (B.L. Xiao), zyma@imr.ac.cn (Z.Y. Ma).

https://doi.org/10.1016/j.jmst.2020.04.016
1005-0302/

rials [15–21], e.g. the SiC continuous fiber/Ti-6Al-4 V composite [15], the NiTi fiber/6082Al composite [16], and the TRIP steels [21]. In most of previous investigations, calculation of load partitioning in a phase relies on the directly measured reflections of this phase from synchrotron X-ray diffraction or neutron diffraction.

For CNT/metal composites, it is almost impossible to obtain clear reflections of the CNTs using synchrotron X-ray diffraction or neutron diffraction for strain determination [10,22,23], because of the following facts. First, the content of CNTs in MMCs is usually small, e.g. lower than 5 vol.% in the CNT/Al composites [24]. Second, CNT is a nano-sized phase that leads to a significant peak broadening effect. Third, only when the normal direction of {002} crystal plane of CNT is parallel to the diffraction vector, the diffraction peak can be detected [25]. Therefore, it is challenging to determine the stress in the CNTs via diffraction methods directly.

In order to reveal the LTSM in the CNT/Al composites, we developed an approach to determine the average stress in the CNTs. In-situ neutron diffraction study on the tensile tests of the 3 vol.% CNT/2009Al composite and the unreinforced 2009Al alloy were performed. The average stresses in the 2009Al matrix and the CNTs were separated. Representative volume element (RVE) based computational homogenization models were employed to simulate stress evolution in the composite.

2. Experimental

2.1. Fabrication of composite

The CNT/2009Al composite was manufactured via a combined process of (a) powder metallurgy (PM), (b) hot forging, (c) friction stir processing (FSP) and (d) rolling. The as-received multi-wall CNTs had 10–15 nm diameter and ~5 μm length. 3 vol.% CNTs were mixed with 2009Al alloy powders with an average 10 μm diameter via a bi-axis rotary mixer at 50 rpm for 8 h with a ball to powder ratio of 2:1. The mixed powders were cold compacted using a cylinder die, degassed to vacuum of 5.0×10^{-3} Pa and hot-pressed at 580 °C into cylindrical composite billet with 75 mm diameter and 75 mm height. An unreinforced 2009Al alloy billet with the same dimension was manufactured using the same PM parameters.

The alloy and the composite billets were hot forged at 450 °C into about 10 mm thick disc-plates. The forged plates were machined to a thickness of about 8 mm and subjected to overlapping FSP under a traveling speed of 50 mm/min and a rotation rate of 1000 rpm. The FSP tool with a concave shoulder 20 mm in diameter and a pin 8 mm in diameter and 6.5 mm in length was used. The tool offset was 2.8 mm between two adjacent FSP passes.

The FSP zones were taken out by machining the surrounding materials away, and then were hot rolled into 1 mm thick sheet at 480 °C along the FSP traveling direction. The rolling reduction for each rolling pass was less than 20 %. After each rolling pass, the CNT/2009Al composite and the 2009Al alloy were annealed at 480 °C for about 30 min. The rolled 2009Al and 3 vol.% CNT/2009Al composite sheets were then heat treated to T4 condition (solution treated at 495 °C for 1 h, water quenched and naturally aged for 7 days). More details about fabrication of the CNT/Al composites using this combined process were reported in our previous investigations [3,10,26,27].

2.2. Transmission electron microscope and electron backscatter diffraction observation

The TEM specimens with a diameter of 3 mm and a thickness of 0.5 mm were cut from the 2009Al alloy and the composite. After mechanical grinding to about 15 μm, the thin foils were subjected to ion bombardment for the final thinning. The microstructure characterization was performed on an FEI Tecnai F20 TEM.

Grain structure of the 2009Al alloy was analyzed by electron backscatter diffraction (EBSD) on a ZEISS SUPRA 55 SEM. The specimen for EBSD was prepared by grinding and mechanical polishing, followed by electro-polishing in a solution with 10 % perchloric acid and 90 % alcohol at −25 °C and 15 V for 1 min.

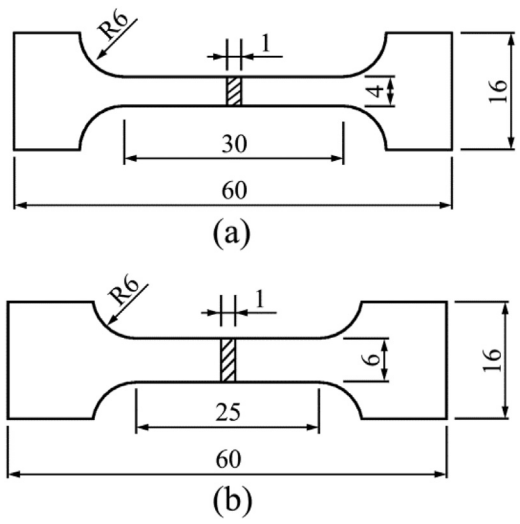

Fig. 1. Geometry and size (mm) of samples: (a) for ex-situ tension tests; (b) for in-situ neutron diffraction.

2.3. Ex-situ tensile tests

Specimens cut from the 2009Al alloy and the composite were used for ex-situ tensile tests in an Instron-5582 tensile machine at room temperature, with a constant strain rate of 1×10^{-3} s^{-1}. Extensometer was used to measure the tensile strain data. The geometry and size of the ex-situ tensile specimens are shown in Fig. 1(a).

2.4. In-situ *neutron diffraction*

In-situ neutron diffraction during tension was conducted at the neutron diffractometer STRESS-SPEC of FRM II. The Si monochromator was selected using the {400} reflection yielding a wavelength of λ =1.67 Å for neutron diffraction. The slit on the incident beam side was 2 mm × 10 mm.

For each type of material, one specimen was used to measure the Al {200} reflection at scattering angle 45°, and another specimen was used to measure the Al {220} reflection at scattering angle 72° and the Al {311}, {222} reflections were at scattering angle 89°. The details about the specimens for in-situ neutron diffraction are listed in Table 1. The geometry and size of the in-situ neutron diffraction specimens are shown in Fig. 1(b). Strains are extracted from the variations of peak positions.

A load frame with a load capacity of ±50 kN was located horizontally on the sample table. The uniaxial tensile tests were performed at room temperature to a strain of about 5%. During in-situ neutron diffraction, all tensile tests were performed in load control (stress holding) mode in the elastic deformation stage, following by displacement control (strain holding) mode at a constant strain rate of 1×10^{-3} s^{-1}. Macroscopic strains were detected using an Instron dynamic extensometer. The in-situ neutron diffraction setup is shown in Fig. 2(a). A neutron diffraction pattern of S3 sample at $2\theta = 89°$ prior to loading is shown in Fig. 2(b), which shows the Al {311} (high intensity) and {222} (low intensity) reflections.

Table 1
In-situ neutron diffraction samples and the measured reflections.

Material name, heat treatment	Samples	Measured reflections of 2009Al	Scattering angle, 2θ
2009Al alloy, T4	S1	{311}, {222}	89°
		{220}	72°
	S2	{200}	45°
3 vol.% CNT/2009Al composite, T4	S3	{311}, {222}	89°
		{220}	72°
	S4	{200}	45°

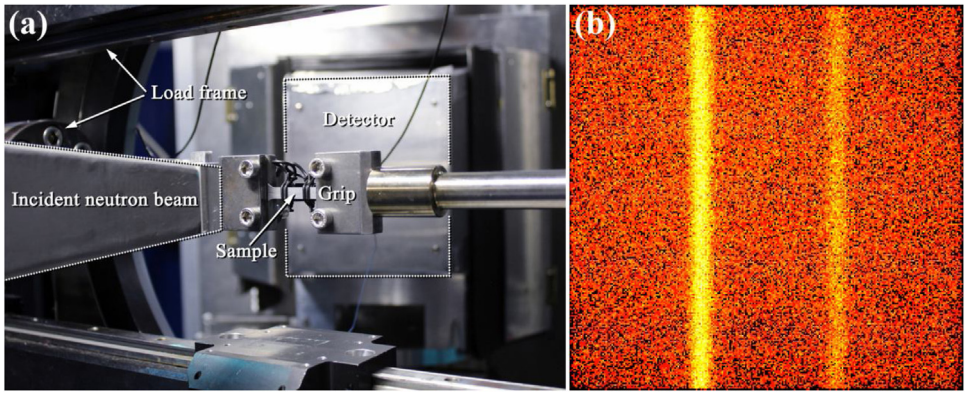

Fig. 2. In-situ neutron diffraction experiment: (a) setup of experiment, where an extensometer was bound on the sample using two black rubber bands; (b) a neutron diffraction pattern.

2.5. Measurement of texture using neutron diffraction

The textures of the 2009Al alloy and the 3 vol.% CNT/2009Al composite were also measured at STRESS-SPEC at MLZ (Garching, Germany). The Ge monochromator was selected using the {311} reflection yielding a wavelength of λ =1.68 Å for the neutron diffraction. The Al {111} and {200} complete pole figures were measured. The orientation distribution function (ODF) was calculated using a series expansion method with an expansion degree of L_{max} = 28.

3. Computational homogenization

Two RVEs of the 3 vol.% CNT/2009Al composite were generated via the software GeoDict (Math2Market GmbH, Germany), as shown in Fig. 3. In the Fiber RVE (Fig. 3(a)), all the CNTs were modeled by generally aligned fibers. In the Fiber-Sphere RVE (Fig. 3(b)), 1.5 vol.% CNTs are modeled by aligned fibers and 1.5 vol.% CNTs are modeled by spheres. The spheres were used to model the CNT clusters. The size of the RVEs was 300 nm × 300 nm × 300 nm. The CNT fibers had a length of 200 nm and a diameter of 15 nm. The CNT spheres had a diameter of 60 nm. The RVEs were discretized into uniform voxel meshes 3 nm in voxel size. Therefore, the meshed RVEs had 100 × 100 × 100 uniform voxels.

The computational homogenization was based on the solution of the following boundary value problem:

$$\nabla \cdot \boldsymbol{\sigma} = 0, \quad \mathbf{x} \in Y \tag{1}$$

$$\mathbf{u} = \boldsymbol{\xi} \cdot \mathbf{x} + \mathbf{u}^*, \quad \mathbf{x} \in \partial Y \tag{2}$$

where Eq. (1) is the equilibrium equation with $\boldsymbol{\sigma}$being the Cauchy stress tensor. Eq. (2) describes the periodic displacement $\mathbf{u}$ at point $\mathbf{x}$ belonging to the boundary ∂Y, and the fluctuation $\mathbf{u}^*$ is periodic.

Table 2
Material parameters used for simulation in the present study.

Material	Parameters	Value
2009Al	Initial yield strength, σ_0	385.0 MPa
	Isotropic hardening modulus, H	700.0 MPa
	Young's modulus	72.4 GPa
	Poisson's ratio	0.33
CNT	Young's modulus	750.0 GPa
	Poisson's ratio	0.20

Y denotes the computational domain, and ∂Y the boundary of the computational domain. The tensor $\boldsymbol{\xi}$ was set as

$$\boldsymbol{\xi} = \begin{bmatrix} 0 & 0 & 0 \\ 0 & \vartheta & 0 \\ 0 & 0 & 0 \end{bmatrix}, \tag{3}$$

where ϑ increases linearly from 0 to a target constant (e.g. 0.05 in the present work). In this work, we adopted the periodic boundary conditions because they are known to provide high accuracy of the target properties even with small RVEs [28].

The 2009Al matrix was modeled by a time-independent J_2-type elasto-plastic constitutive law with an isotropic hardening rule that reads [29]

$$\sigma(\varsigma) = \sigma_0 + H\varsigma, \tag{4}$$

where $\varsigma$is the accumulated plastic strain, σ_0 the initial yield strength, and H the isotropic hardening modulus. The material parameters of the 2009Al matrix are listed in Table 2.

The CNTs were modeled by a linear elastic constitutive law. The ideal Young's modulus of single-walled CNTs is up to 1000 GPa [30,31], and that of multi-walled CNTs ranges from 270 to 950 GPa [32]. It is noted that the Young's modulus of the CNTs depends on both the types and the number of defects [33,34]. In the present work, the CNTs were partially damaged during manufacturing. Therefore, a reasonable value of 750 GPa was set for the Young's modulus of multi-walled CNTs. The Poisson's ratio of

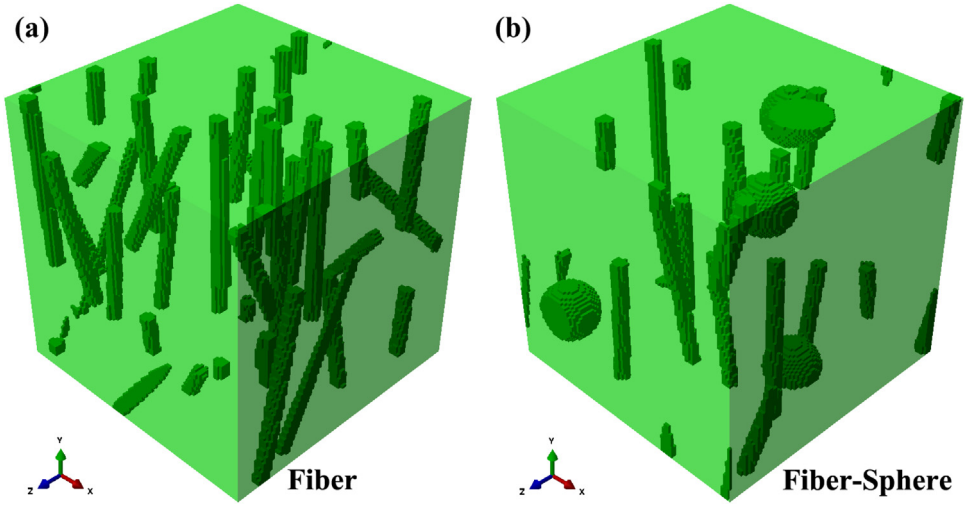

Fig. 3. RVEs used for simulation of 3 vol.% CNT/2009Al composites: (a) all CNTs are modeled by generally aligned fibers, named as Fiber RVE; (b) 1.5 vol.% CNTs are modeled by aligned fibers and 1.5 vol.% CNTs are modeled by spheres, named as Fiber-Sphere RVE.

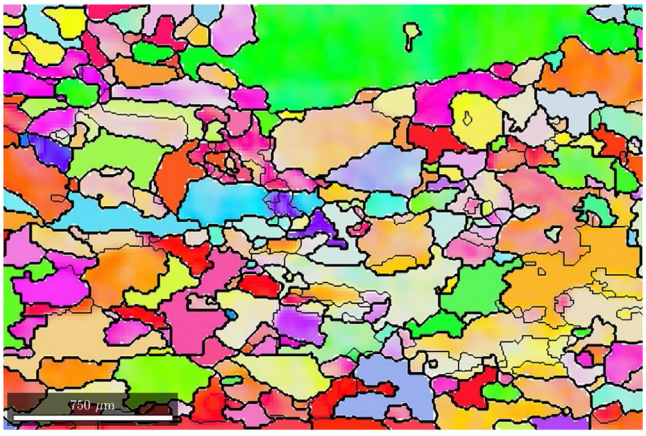

Fig. 4. Grain structure of the 2009Al alloy determined via EBSD.

CNTs was set to 0.20 [35]. In the present model, the CNTs (fibers in Fig. 3(b)) and the CNT clusters (spheres in Fig. 3(b)) are modeled by the same elastic constitutive law.

The computational homogenization model was solved by ABAQUS. During post processing, the averaged stresses in the 2009Al matrix $\langle\sigma\rangle_{2009Al}$ and CNTs $\langle\sigma\rangle_{CNTs}$ are calculated via the following homogenization method

$$\langle\sigma\rangle_i = \frac{1}{V_i}\int_{\omega_i}\sigma d\omega, \tag{5}$$

$$V_i = \int_{\omega_i} d\omega, \tag{6}$$

$$\sum_i V_i = \int_Y dY, \tag{7}$$

where V_i is the phase volume, ω_i the phase domain, and i = 2009Al or CNTs.

4. Results and discussion

4.1. Microstructures

The grain structure of the 2009Al alloy is shown in Fig. 4. Generally, the grains had elongated shape with long axis parallel to the rolling direction. The average length and width of the grains were 178.3 and 91.1 μm, respectively. In Fig. 4, a large grain with 2151.3 μm length and 619.6 μm width was observed, which formed due to recrystallization during annealing treatment.

Fig. 5(a) shows that the grain size of the matrix in the 3 vol.% CNT/2009Al composite was from ~0.1 to ~0.4 μm. It can be seen that the CNTs caused significant grain refinement, agreeing with previous works [2,10,23,36]. The CNTs distribution in the composite is shown in Fig. 5(b). The CNTs were cut into short nanotubes with lengths from ~0.1 to ~0.3 μm. The dispersed CNTs aligned along the rolling direction (RD) generally. In addition, some CNT clusters were observed, which had an average diameter of about 60 nm.

4.2. Textures

Fig. 6 shows the calculated ODF $\varphi_1 - \Phi$ (Bunge notation [37]) at three φ_2 values (0°, 45° and 65°). It can be seen that both materials had three texture components, including the Brass {110}<112>, the S {123}<643> and the Rotated Cube {001}<110> components. The Brass {110}<112> and the S {123}<643> components are characteristic rolling texture components in the FCC metals. The Rotated Cube {001}<110> component is a characteristic recrystallization texture component in the FCC metals.

The intensities of three texture components had some differences between the alloy and the composite. The alloy was dominated by the Brass {110}<112> deformation component with peak intensity of 14.7 MRD, while the S {123}<643> and the Rotated cube {001}<110> components were relatively weak. The composite was dominated by the Rotated cube {001}<110> recrystallization component with peak intensity of 4.6 MRD. Meanwhile, the other two texture components were also strong. These results revealed that the addition of CNTs stimulated the recrystallization in the composite during the annealing treatments between rolling passes.

4.3. Macroscopic true stress-strain curves

The macroscopic stress–strain curves of all in-situ tensile specimens are shown in Fig. 7(a). A typical stress relaxation phenomenon was observed in all specimens during neutron diffraction measurement period with strain holding. Such a stress relaxation phenomenon can also be found in other in-situ neutron diffraction experiments during strain holding [38,39]. Fig. 7(b) shows the average stress–strain curves during in-situ neutron diffraction,

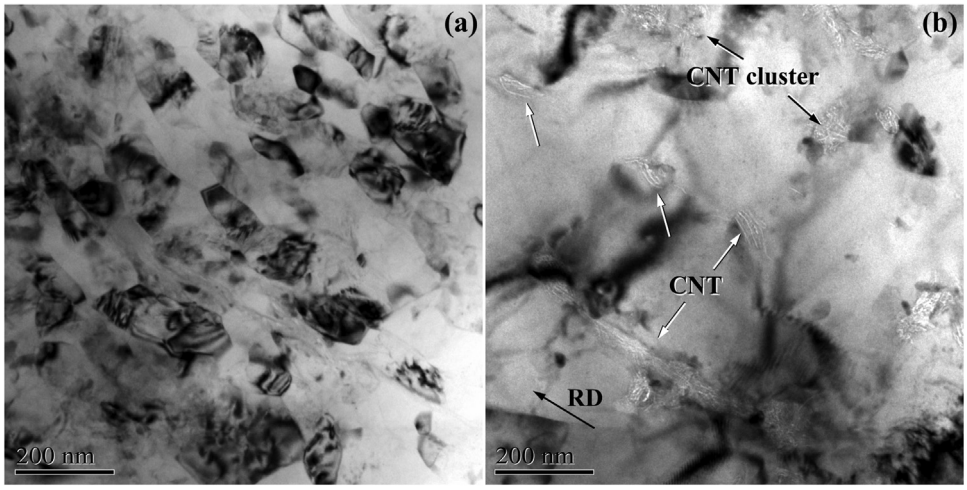

Fig. 5. TEM images of the 3 vol.% CNT/2009Al composite: (a) grain structure; (b) CNT distribution.

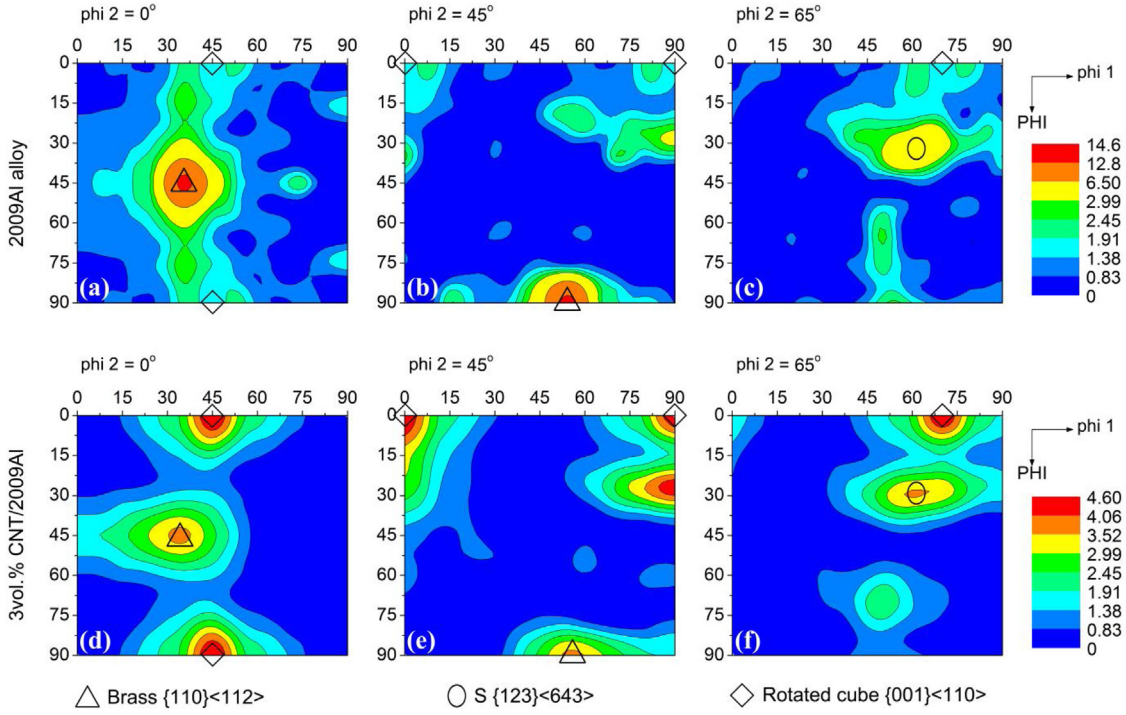

Fig. 6. ODF results of the 2009Al alloy and the 3 vol.% CNT/2009Al composite.

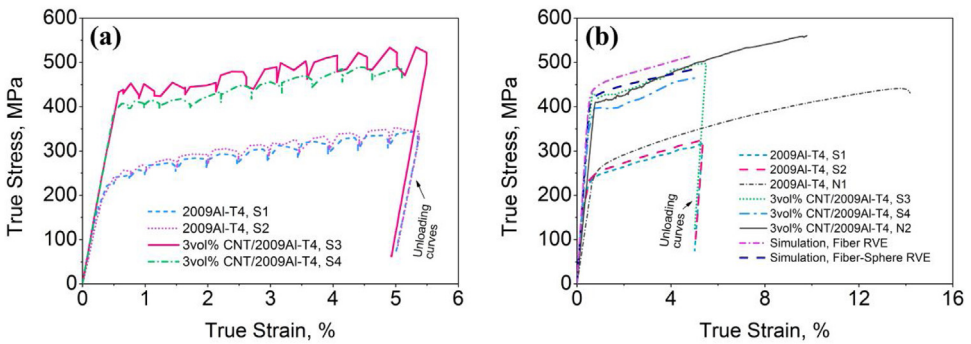

Fig. 7. Macroscopic stress vs. strain curves: (a) as-recorded curves during in-situ neutron diffraction; (b) average stress-strain curves from in-situ experiments (S1–S4), the stress–strain curves from ex-situ experiments (N1 and N2), and the simulated curves.

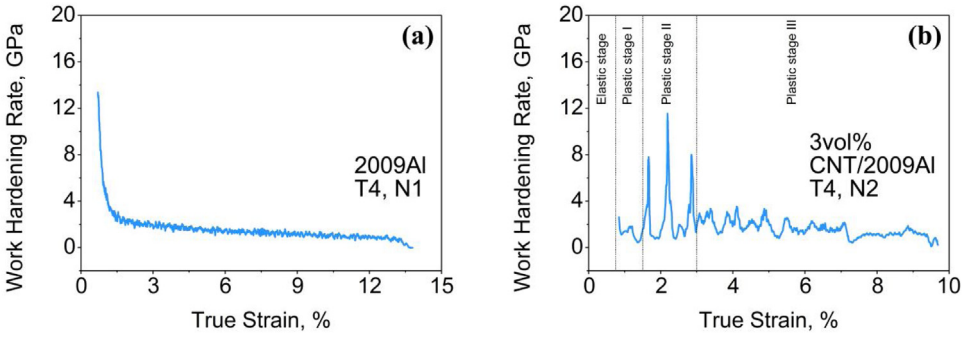

Fig. 8. Comparison of work-hardening rate during plastic deformation as a function of true strain between the 2009Al-T4 sample N1 and the 3 vol.% CNT/2009Al-T4 sample N2.

as well as the stress–strain curves measured via ex-situ tensile tests, denoting by "2009Al-T4, N1" and "3 vol.% CNT/2009Al-T4, N2", respectively. Similar to the Ref. [40], the average stress–strain curves were obtained through time-average method. It can be seen that with the addition of CNTs the average increase in the yield strength of the composites was about 180 MPa. Fig. 7(b) reveals that the elongation of the N1 2009Al alloy specimen was 15 %, while that of the N2 composite specimen was reduced to 10 %.

The stress–strain curves predicted by the computational homogenization model are also plotted in Fig. 7(b). The predicted stress–strain curve based on the Fiber-Sphere RVE matched with the measured curves of the composite specimens, especially the S3 specimen. The predicted stress–strain curve based on the Fiber RVE was about 18 MPa higher than that predicted by the Fiber-Sphere RVE.

Fig. 8(a) shows that the work hardening rate of the 2009Al alloy decreased continuously with increasing the applied strain. Differently, Fig. 8(b) shows that the work hardening rate of the composite had abnormal characteristics, which was determined from the fluctuation of stress-strain curve of the composite, i.e. "3 vol.% CNT/2009Al-T4, N2" in Fig. 7(b). Similar fluctuations of stress-strain curves were also reported in previous works [3,41]. This behavior is probably caused by local plastic deformation due to the fine grain size. As observed in previous works [42–44], local plastic deformation, e.g. the Portevin-Le Chatelier band, is favored in Al alloys with submicron grains. As pointed out by Yilmaz [43], the mechanism of the Portevin-Le Chatelier band is quite complex, which is related to the dislocation–dislocation interaction or the dislocation-solute interaction.

According to the characteristics of the work hardening rate curve, the plastic deformation of the composite can be divided into three stages: stage I from strain 0.07%–1.5%, stage II from strain 1.5%–3.0%, and stage III after strain 3.0 %, as marked in Fig. 8(b). The work hardening rate of the composite in stage I had small variation. The corresponding stress–strain curves of the composite specimens S3, S4 and N2 in Fig. 7(b) exhibited a stress plateau in stage I. In stage II, the work hardening rate curve had three major peaks [42,43,45]. In stage III, the work hardening rate exhibited low values with multiple peaks. According to those characteristics, local plastic deformation occurred in the composite [44,46].

4.4. Lattice strains, stress partition and load transfer mechanism

Fig. 9 shows the lattice strains in the 2009Al alloy and the 2009Al matrix of the composite as a function of the applied strain. The lattice strains in the 2009Al matrix were higher than those in the 2009Al alloy. This indicates higher strength of the 2009Al matrix. Fig. 9(a)–(d) shows that the lattice strains of the 2009Al alloy increased continuously after yielding. However, in the 2009Al matrix the lattice strains decreased after the yielding point until the applied strain of 1.5 %. The drop of the Al {311} lattice strain was larger than those of the {220} and {222} lattice strains (Fig. 9(b) and (c)). This reveals an anisotropic microscopic plastic deformation behavior.

Recalling the three plastic stages of the composite (Fig. 8(b)), the reduction in lattice strains in Fig. 9 was attributed to local plastic deformation in stage I. Recently, Zhang et al. [44] also observed a significant reduction in the austenite {311} lattice strain in a medium-Mn steel due to the propagation of Lüders band.

To characterize the LTSM quantitatively, the stresses in the 2009Al matrix and the CNTs need to be separated. For this purpose, appropriate reflections of the 2009Al matrix need to be selected. Previous theoretical work by Clausen et al. [47] has shown that the {311} lattice strain and the applied stress have a linear relationship during both elastic and plastic deformation in FCC alloys. For this reason, the {311} reflection is the most recommended one for characterizing stresses and strains for FCC alloys. Other recommended reflections for FCC alloys are the {422} and {220} reflections. In contrast, the {200} reflection is problematic for FCC materials because it is measured at a small diffraction angle and is strongly affected by intergranular strains [47,48].

It should be noted that the approximate linear response of the recommended reflections to the applied stress is not always valid during plastic deformation, especially in multiphase materials (like composites). The nonlinearity is mainly caused by load transfer from the soft and compliant phase (usually the matrix) to the stiff and hard phase (usually the reinforcement) [18,21]. Compared with the materials including large sized reinforcements (e.g. larger than several microns), the materials including nano-sized reinforcements have stronger nonlinearity in the lattice strain vs. applied stress curve of recommended reflections. For instance, in an Fe–Cr–Ni–Al–Ti alloy strengthened by nano-sized hierarchical-Ni2TiAl/NiAl particles, the slope of the recommended reflection {110} for the BCC structured ferritic matrix changed significantly during plastic deformation, with the partitioned load in the nano-sized particles increasing rapidly [49].

As shown in Fig. 10(a), the {311} lattice strain vs. applied stress curve of the 2009Al alloy had an ideal linear relationship during elastic deformation and a slightly nonlinear relationship during plastic deformation. The {311} lattice strain vs. applied stress curve of the 2009Al matrix (S3 specimen) had a linear relationship during elastic deformation and a strong nonlinear relationship during plastic deformation. In the elastic stage, at the same applied stress the {311} lattice strain in the 2009Al matrix was lower than that in the 2009Al alloy, proving the existence of the load transfer mechanism. Besides, Fig. 10(a) reveals that for the 2009Al matrix the slope of the curve increased when the applied stress increased from 309 to 432 MPa. This phenomenon was caused by the onset of local plastic deformation.

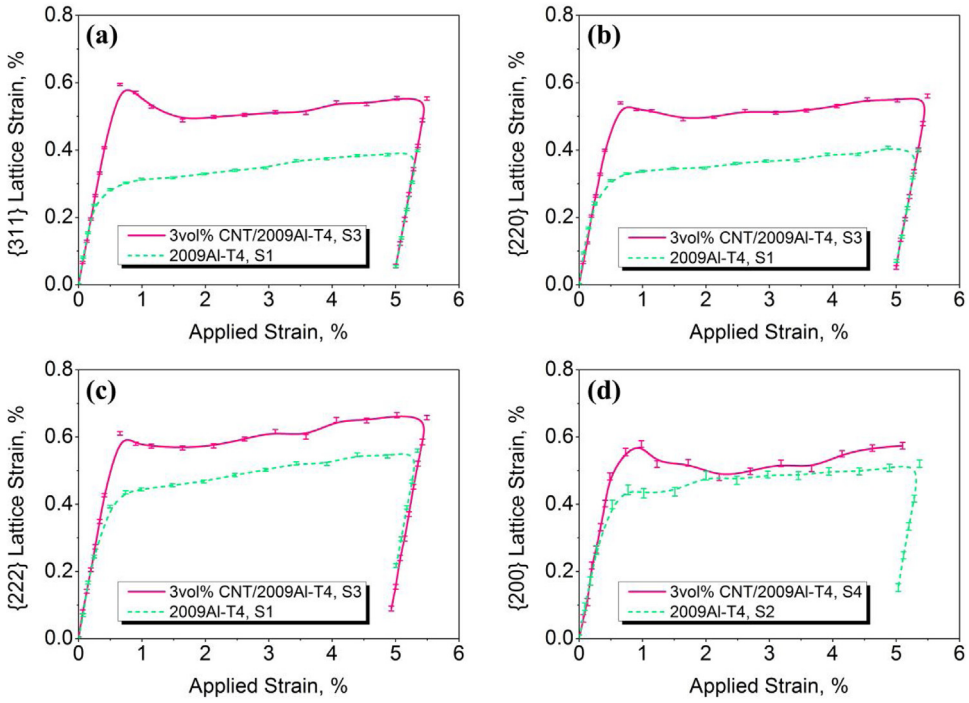

Fig. 9. Lattice strain vs. applied strain curves of the 2009Al alloy and the 3 vol.% CNT/2009Al composite. Error bars of the measured lattice strains are shown for all curves.

Based on the data in Fig. 10(a), the average stresses in the 2009Al matrix and the CNTs can be separated. The average stress in the CNTs can be calculated based on the diffraction elastic constants (DECs) and the stress equilibrium condition. For uniaxial deformation of homogeneous alloys, the lattice strain $\varepsilon_{\{hkl\}}$ along the loading direction (LD) of $\{hkl\}$ lattice plane relates to the applied stress σ^{LD} and the DEC $E^{\mathrm{LD}}_{\{hkl\}}$ as [50,51]:

$$\varepsilon^{\mathrm{LD}}_{\{hkl\}} = \frac{\sigma^{\mathrm{LD}}}{E^{\mathrm{LD}}_{\{hkl\}}} \tag{8}$$

From Eq. (8), the DEC $E^{\mathrm{LD}}_{\{hkl\}}$ of the 2009Al alloy can be calculated easily via

$$E^{\mathrm{LD}}_{\{hkl\}} = \frac{\sigma^{\mathrm{LD}}}{\varepsilon^{\mathrm{LD}}_{\{hkl\}}} \tag{9}$$

The 2009Al alloy and the 2009Al matrix in the CNT/2009Al composite should have the same DEC for the same $\{hkl\}$ lattice plane, because they have the same chemical composition and almost the same texture. In addition, the elastic anisotropy of Al is weak, which could reduce the influence of texture. Therefore, the {311} DEC of the 2009Al alloy should be identical to that of the 2009Al matrix in the composite. Based on this assumption, the average stress in the 2009Al matrix of the composite can be evaluated approximately.

The {311} DEC of the 2009Al alloy was determined by linear fitting of the applied stress vs. lattice strain data of the alloy, as shown in Fig. 10(a). The determined $E^{\mathrm{LD}}_{\{311\}}$ of the 2009Al alloy was 72.36 GPa, which was very close to the macro Young's modulus for Al alloys, in accordance with Ref. [52]. Similarly, the {220} DEC of the 2009Al alloy was determined to be 70.81 GPa, as shown in Fig. 10(b). Fig. 10(c) and (d) shows the Al {222} and {200} lattice strains with respect to the applied stress. At the same applied stress, the {222} and {200} lattice strains in the 2009Al matrix of the composite were generally smaller than those in the 2009Al alloy, proving the existence of the LTSM.

With the determined $E^{\mathrm{LD}}_{\{311\}}$ and $E^{\mathrm{LD}}_{\{220\}}$, subsequently, the average stress in the 2009Al matrix of the composite, $\sigma^{\text{Al-matrix}}$, can be calculated by

$$\sigma^{\text{Al-matrix}} = E^{\mathrm{LD}}_{\{hkl\}}\varepsilon_{\{hkl\}} \tag{10}$$

The determined values of $\sigma^{\text{Al-matrix}}$ based on the Al {311} and {220} reflections are plotted by the black short dash line in Fig. 10(a) and (b), respectively.

The average stresses in the 2009Al matrix $\sigma^{\text{Al-matrix}}$ and CNTs σ^{CNT} have a relation to the total applied stress of the composite along the loading direction, σ^{Total}, which is called the stress equilibrium condition

$$\sigma^{\mathrm{Total}} = (1 - V_{\mathrm{CNT}})\sigma^{\text{Al-matrix}} + V_{\mathrm{CNT}}\sigma^{\mathrm{CNT}} \tag{11}$$

where V_{CNT} is the volume fraction of CNTs. Now, the average stress in the CNTs can be extracted by

$$\sigma^{\mathrm{CNT}} = \frac{1}{V_{\mathrm{CNT}}}\left[\sigma^{\mathrm{Total}} - (1 - V_{\mathrm{CNT}})\sigma^{\text{Al-matrix}}\right] \tag{12}$$

The average stresses in the CNTs σ^{CNT} determined based on the measured Al {311} and {220} lattice strains are plotted in Fig. 11(a). The determined values of σ^{CNT} based on the Al {311} and {220} lattice strains were very close to each other. In order to minimize the errors, the determined values of σ^{CNT} were linearly fitted. The fitted line in Fig. 11(a) indicated that the average stress in the CNTs σ^{CNT} reached 1630 MPa at the yield strength (432 MPa) of the composite.

The average stress in the CNTs can also be calculated from the RVE based computational model. The predicted average stress in the CNTs using the Fiber-Sphere RVE is shown in Fig. 11(a), which agreed well with the measured stress in the CNTs σ^{CNT}. As expected, the predicted average stress in the CNTs based on the Fiber RVE was higher because stronger load transfer effect can be captured in this model. Moreover, both predicted stress–strain curves (Fig. 11(a)) from the computational homogenization model show that after macroscopic yielding, the average stress in the CNTs increased rapidly. This dramatic stress increase behavior of the reinforcements during plastic deformation was also observed in

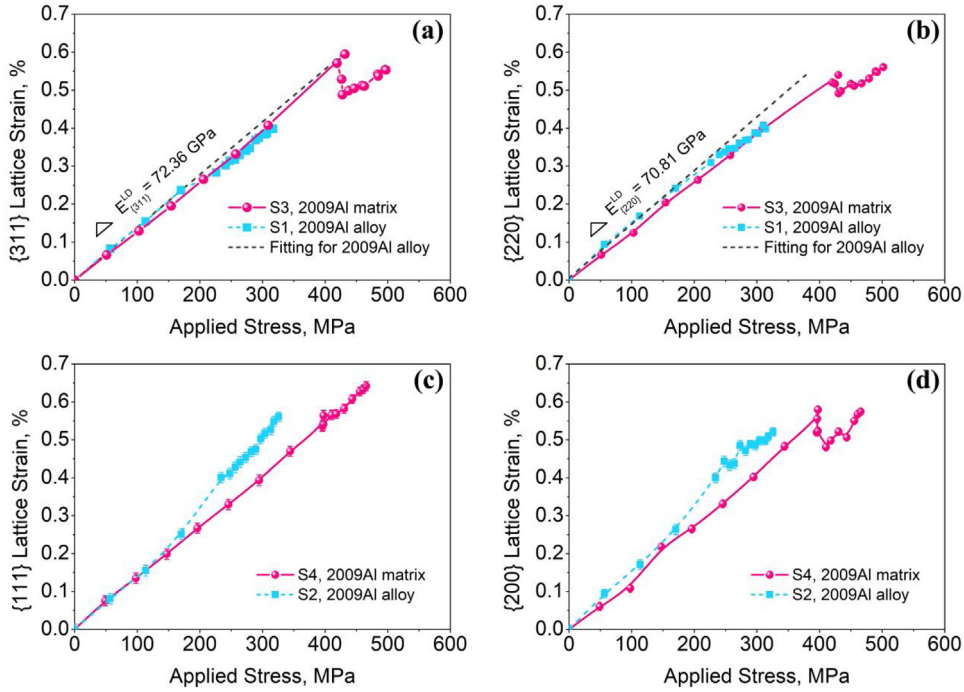

Fig. 10. Evolution of lattice strains as a function of applied stress in both the 2009Al matrix of the composite and the 2009Al alloy: (a) {311} lattice strains, (b) {220} lattice strain, (c) {111} lattice strain and (d) {200} lattice strain.

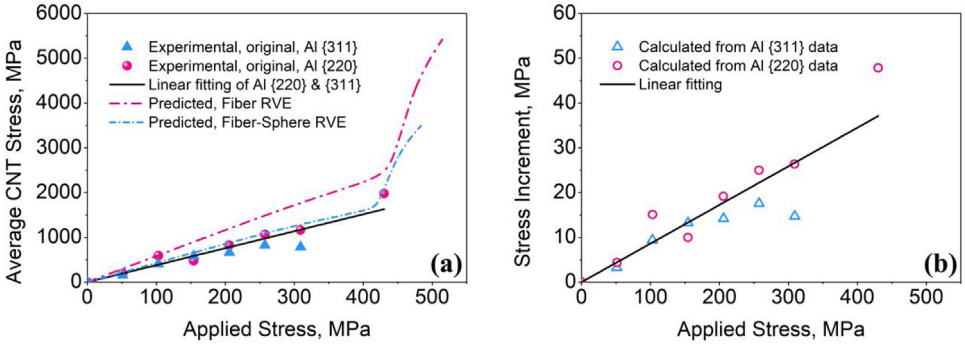

Fig. 11. Load transfer mechanism in the 3 vol.% CNT/2009Al composite: (a) average stress in CNTs; (b) stress increment of the composite during elastic deformation stage.

the (Al_2O_3+Si)/Al composite through synchrotron X-ray diffraction experiment [53].

Due to load transfer from the 2009Al matrix to the CNTs, the average stress in the composite increases. The stress increment of the composite due to the CNTs, $\sigma^{\mathrm{CNT}}_{\mathrm{strelncre}}$, can be calculated simply by

$$\sigma^{\mathrm{CNT}}_{\mathrm{strelncre}} = \sigma^{\mathrm{Total}} - \sigma^{\mathrm{Al\text{-}matrix}} \tag{13}$$

The calculated values of $\sigma^{\mathrm{CNT}}_{\mathrm{strelncre}}$ based on the Al {311} and {220} reflections are shown in Fig. 11(b). The scattered data were then linearly fitted, indicating that the yield strength of the 3 vol.% CNT/2009Al composite increased about 37 MPa due to the LTSM.

For cylindrical fibers or whiskers reinforced composites, the yield strength of the composites σ^{y}_{com} can be estimated based on the modified shear lag model by [54]

$$\sigma^{\mathrm{y}}_{\mathrm{com}} = \sigma^{\mathrm{y}}_{\mathrm{ma}}\left[\frac{s+2}{2}V_{\mathrm{re}} + (1 - V_{\mathrm{re}})\right] \tag{14}$$

where $\sigma^{\mathrm{y}}_{\mathrm{ma}}$ denotes the yield strength of the matrix, s the aspect ratio of the reinforcement, V_{re} the volume fraction of the reinforcement. From Eq. (14), one can easily calculate the contribution of the LTSM $\Delta\sigma_{\mathrm{lt}}$ by

$$\Delta\sigma_{\mathrm{lt}} = \sigma^{\mathrm{y}}_{\mathrm{com}} - \sigma^{\mathrm{y}}_{\mathrm{ma}} = \frac{1}{2}\sigma_{\mathrm{ma}}V_{\mathrm{re}}s \tag{15}$$

Eq. (15) shows that with a given yield strength of the matrix the increase in yield strength of the composite due to load transfer depends on the volume fraction and the aspect ratio of the CNTs. If the CNTs are well dispersed in the Al matrix, have large aspect ratio and bond with the Al matrix well, the load transfer effect should be stronger.

The average stresses in the matrix determined via Eq. (10) as a function of the applied strain are shown in Fig. 12, which were calculated based on the measured Al {311} and {220} lattice strains. Furthermore, the corresponding predicted average stress vs. applied strain curves are also shown in Fig. 12. Except in the early plastic deformation stage the two experimental curves coincided to each other. Generally, the predicted average stress vs. applied strain curves agreed with the experimental curves. As expected, the predicted curve based on the Fiber RVE was lower than that based on the Fiber-Sphere RVE because stronger load transfer effect was captured in the Fiber RVE model.

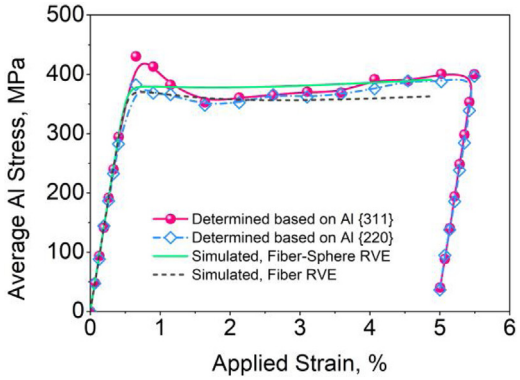

Fig. 12. Average stress in the 2009Al matrix as a function of the applied strain.

The predicted Mises stress fields in each phase of the two RVEs are shown in Fig. 13. At least three features can be observed. Firstly, as shown in Fig. 13(a) and (c), the stress concentration position in the matrix was located near the CNT ends. The Mises stresses in the matrix near the middle of the CNTs were relatively smaller. Differently, as shown in Fig. 13(b) and (d), in the CNTs, the stress concentration position was located near the middle of length, while the stresses near the CNT ends were relatively smaller. Such heterogeneous distribution of stress was mainly caused by the LTSM [54]. Secondly, Fig. 13(a) and (c) show that the Mises stresses in the gray colored regions were smaller than 385 MPa, i.e. still in elastic state. This reveals that the deformation of the matrix at microscale was heterogeneous. Thirdly, Fig. 13(b) shows that the CNTs whose long axis was not parallel to or not near the loading direction had lower stresses. Fig. 13(d) shows that the spheres had much lower stresses compared with fibers. These results indicate that in order to efficiently utilize the superior mechanical properties, the CNTs should be well dispersed and aligned along the loading direction.

The above results reveal that the LTSM contributes a small portion to the total increment of the yield strength (~180 MPa) of the composite in the present case. Most increment of the yield strength is caused by additional strengthening mechanisms. Section 4.1 shows that the grain refinement of the Al matrix is one important strengthening mechanism. Furthermore, as revealed by Chen et al. [55], the strengthening mechanism of CNT/Al composites depends on the aspect ratio of CNTs. When the CNTs have an aspect ratio smaller than 10, the strengthening mechanism is dominated by the Orowan looping mechanism. When the CNTs have an aspect ratio over 40, the LTSM dominates the strengthening mechanism. When the CNTs have an aspect ratio between 10 and 40, there is a transition from the Orowan looping mechanism to the LTSM [55]. For the 1.3 vol.% CNT/Al composites with different CNT aspect ratios (from 6.5 to 55) in Ref. [55], increments of the yield strengths due to the LTSM of the CNTs are in the range from 4.3 to 36.2 MPa.

With the above approach developed in this work, it is possible to track the load transfer effect of the CNTs during loading of their MMCs. The LTSM of the CNTs in their MMCs can be assessed experimentally. This will help researchers to optimize practical methods for maximum utilization of the spectacular mechanical properties of the CNTs, resulting in development of new high-performance MMCs reinforced by the CNTs in the future.

Evolution of full width at half maximum (FWHM) of diffraction reflection

The determined FWHM includes three contributions: the instrument, the grain size and the micro-stresses (mainly due to dislocations). The determined FWHM as a function of 2θ in Fig. 14(a) were used to calibrate the measured FWHM of different specimens. At scattering angles between 75° and 90°, the STRESS-SPEC

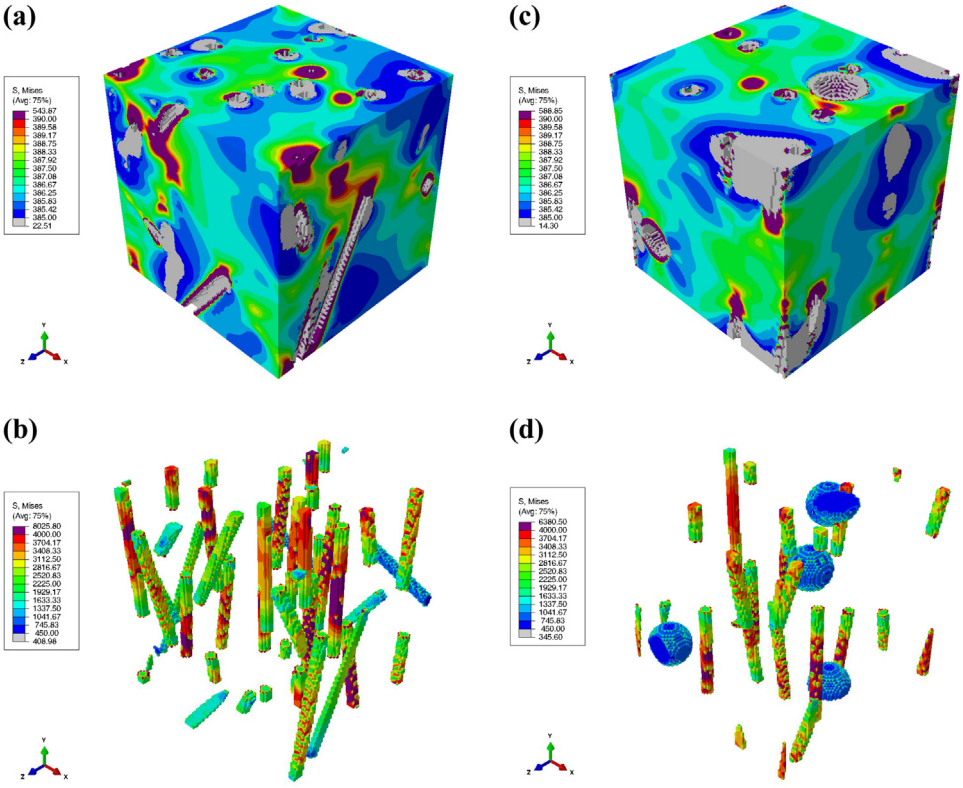

Fig. 13. Predicted Mises stress (MPa) fields at the 0.7 % applied strain: (a) in the matrix and (b) the CNTs of the Fiber RVE; (c) in the matrix and (d) the CNTs of the Fiber-Sphere RVE. The tension loading direction is along the Y-axis, i.e. the vertical direction.

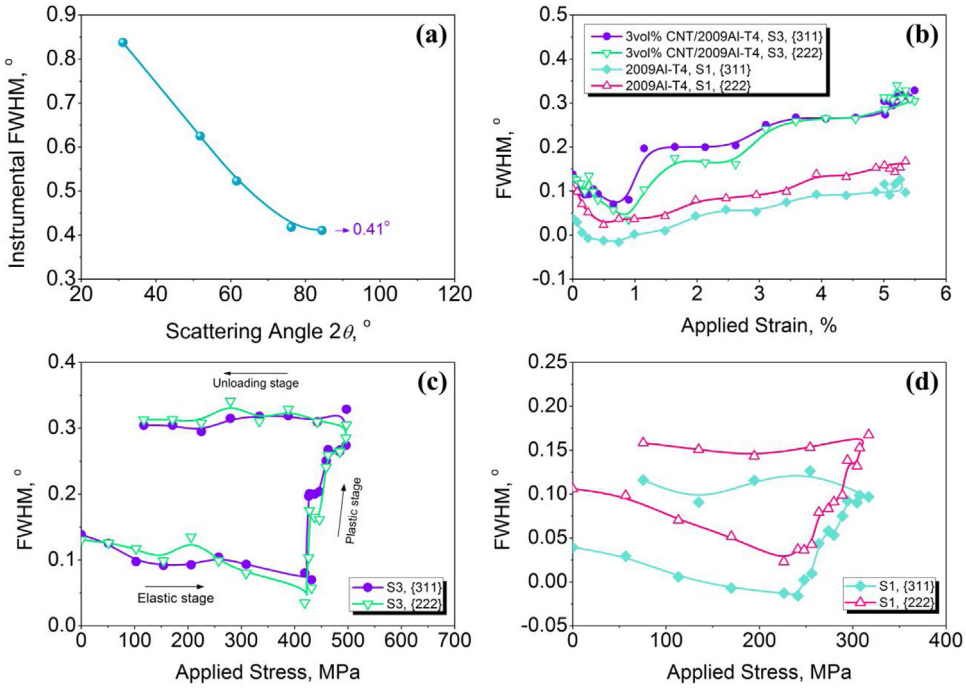

Fig. 14. Evolutions of FWHM: (a) instrumental FWHM at different scattering angles measured using a standard Si powder; (b) FWHM vs. applied strain curves of different materials; FWHM vs. applied stress curves of (c) the composite and (d) the alloy.

diffractometer had the lowest instrumental FWHM, with a value of 0.41°. Therefore, at the scattering angle of about 90°, the Al {311} and {222} reflections for all specimens were used to characterize the FWHM. The values of FWHM plotted in Fig. 14(b)–(d) were obtained using the original FWHM of the fitted peaks subtracting 0.41°.

From the FWHM vs. applied strain curves in Fig. 14(b), it can be seen that the FWHM of the 2009Al matrix in the composite was larger than that of the 2009Al alloy. With the addition of the CNTs, the composites had much smaller grain size than the unreinforced Al alloys, agreeing with previous observations [2,10]. Previous investigations have shown that the dislocation density is inversely proportional to the grain size (when the grain size is no less than several tens of nanometer) during plastic deformation [56–59]. Therefore, at the same applied strain the dislocation densities in the CNT/Al composites should be higher than those in the unreinforced Al alloys. Besides, the CNTs act as stiff obstacles to dislocations during plastic deformation, which leads to an increase in dislocation density.

The FWHM-applied stress plots in Fig. 14(c) and (d) clearly show that the evolution of FWHM had three stages, i.e. an elastic stage, a plastic stage and an unloading stage. During elastic deformation, a few dislocations start to move within short distances when the shear stress in the Burgers vector direction is higher than the Peierls stress [60,61]. If neighboring dislocations with opposite natures (positive and negative) encounter and vanish, the dislocation density reduces and the FWHM values decrease slightly. Similar phenomenon in a 7020Al-T6 alloy was observed by Zhong et al. [61]. During plastic deformation, multiplication of dislocations leads to an increase in dislocation density. Therefore, FWHM increased with the applied stress during plastic deformation. The flow stress σ_f relates to the dislocation density ρ through the Taylor model [62]

$$\sigma_f = \sigma_0 + \overline{M}\alpha\mu b\sqrt{\rho} \tag{16}$$

where σ_0 is the friction stress, $\overline{M}$ the average Taylor factor, α a material constant, μ the shear modulus and b the Burgers vector. Therefore, as shown in Fig. 14(c)-and (d), FWHM increased rapidly with increasing the applied stress. When the specimens were unloaded, the dislocations were stored in the specimens, resulting in a nearly constant FWHM.

5. Conclusions

(1) The 2009Al alloy and the CNT/Al composite exhibited the same type of texture, including the Brass {110}<112 >, the S {123}<643> and the Rotated cube {001}<110> components. The CNTs stimulated the recrystallization in the composite during the annealing treatments.

(2) In the elastic deformation, the lattice strains in the 2009Al matrix were smaller than those in the 2009Al alloy, proving the existence of the LTSM. The 2009Al {311} and {220} DECs were determined to be 72.36 and 70.81 GPa, respectively. The average stress in the 2009Al matrix of the composite can be calculated using the DECs.

(3) The determined average stress in the CNTs indicates that the value reached up to 1630 MPa at the yield strength of the composite (432 MPa) based on linear regression of the measured data. The LTSM contributed to an increment of yield strength by about 37 MPa. The predicted average stress in the CNTs from the computational model agreed with measured data during elastic stage, and increased rapidly during plastic stage.

(4) The FWHM of the 2009Al matrix and the 2009Al alloy decreased slightly during elastic stage, and increased sharply during plastic stage due to increase in dislocation density. During plastic stage, the absolute FWHMs and their increments of the selected lattice planes in the 2009Al matrix were higher than those in the 2009Al alloy at a given strain.

Acknowledgments

This work was financially supported by the National Key R&D Program of China (No. 2017YFB0703104), the National Natural Science Foundation of China (Nos. 51871214 and 51931009) and the

"Key Research Program of Frontier Sciences, CAS" (No. QYZDJ-SSW-JSC015). This work is based upon experiments performed at the STRESS-SPEC instrument operated by TUM, TU Clausthal and GEMS at the Heinz Maier-Leibnitz Zentrum (MLZ), Garching, Germany. The authors are very grateful to the staff of FRM II, Garching, Germany for their kind support of the experiments on their sites. The authors are also very grateful to the PhD students C. Yang and K. Ma for their helps in fabrication of the materials and TEM characterization.

References

[1] Z.Q. Tan, Z.Q. Li, G.L. Fan, W.H. Li, Q.L. Liu, W. Zhang, D. Zhang,Nanotechnology 22 (2011), 225603.
[2] D.H. Nam, S.I. Cha, B.K. Lim, H.M. Park, D.S. Han, S.H. Hong, Carbon 50 (2012) 2417–2423.
[3] Z.Y. Liu, B.L. Xiao, W.G. Wang, Z.Y. Ma, Carbon 62 (2013) 35–42.
[4] A. Azarniya, A. Azarniya, S. Sovizi, H.R.M. Hosseini, T. Varol, A. Kawasaki, S. Ramakrishna, Prog. Mater. Sci. 90 (2017) 276–324.
[5] R. George, K.T. Kashyap, R. Raw, S. Yamdagni, Scr. Mater. 53 (2005) 1159–1163.
[6] B. Chen, S.F. Li, H. Imai, L. Jia, J. Umeda, M. Takahashi, K. Kondoh, Compos. Sci. Technol. 113 (2015) 1–8.
[7] W.W. Zhou, G. Yamamoto, Y. Fan, H. Kwon, T. Hashida, A. Kawasaki, Carbon 106 (2016) 37–47.
[8] S.E. Shin, D.H. Bae, Mater. Charact. 83 (2013) 170–177.
[9] S.H. Dong, J.Q. Zhou, D. Hui, Y. Wang, S. Zhang, Compos. Pt. A-Appl. Sci. Manuf. 68 (2015) 356–364.
[10] Z.Y. Liu, B.L. Xiao, W.G. Wang, Z.Y. Ma, Carbon 50 (2012) 1843–1852.
[11] K.T. Kim, J. Eckert, S.B. Menzel, T. Gemming, S.H. Hong,Appl. Phys. Lett. 92 (2008), 121901.
[12] L.J. Huang, L. Geng, H.X. Peng, Prog. Mater. Sci. 71 (2015) 93–168.
[13] L.J. Huang, L. Geng, A.B. Li, F.Y. Yang, H.X. Peng, Scr. Mater. 60 (2009) 996–999.
[14] I.A. Kinloch, J. Suhr, J. Lou, R.J. Young, P.M. Ajayan, Science 362 (2018) 547–553.
[15] P.J. Withers, A.P. Clarke, Acta Mater. 46 (1998) 6585–6598.
[16] W.D. Armstrong, T. Lorentzen, P. Brondsted, P.H. Larsen, Acta Mater. 46 (1998) 3455–3466.
[17] M.L. Young, J.D. Almer, M.R. Daymond, D.R. Haeffner, D.C. Dunand, Acta Mater. 55 (2007) 1999–2011.
[18] N. Jia, R.L. Peng, D.W. Brown, B. Clausen, Y.D. Wang, Metall. Mater. Trans. A 39 (2008) 3134–3140.
[19] T.E. Wilkes, B.J. Harder, J.D. Almer, K.T. Faber, Acta Mater. 57 (2009) 6234–6242.
[20] M.L. Young, R. Rao, J.D. Almer, D.R. Haeffner, J.A. Lewis, D.C. Dunand, Acta Mater. 57 (2009) 2362–2375.
[21] S. Harjo, N. Tsuchida, J. Abe, W. Gong, Sci. Rep. 7 (2017) 15149.
[22] S. Suarez, E. Ramos-Moore, F. Mucklich, Carbon 51 (2013) 404–409.
[23] F. Mokdad, D.L. Chen, Z.Y. Liu, B.L. Xiao, D.R. Ni, Z.Y. Ma, Carbon 104 (2016) 64–77.
[24] S.C. Tjong, Mater. Sci. Eng. Res. 74 (2013) 281–350.
[25] A.Y. Cao, C.L. Xu, J. Liang, D.H. Wu, B.Q. Wei, Chem. Phys. Lett. 344 (2001) 13–17.
[26] K. Zhao, Z.Y. Liu, B.L. Xiao, D.R. Ni, Z.Y. Ma, Acta Metall. Sin. (Engl. Lett.) 31 (2017) 134–142.
[27] K. Zhao, Z. Liu, B. Xiao, Z. Ma, J. Mater. Sci. Technol. 33 (2017) 1004–1008.
[28] S. Bargmann, B. Klusemann, J. Markmann, J.E. Schnabel, K. Schneider, C. Soyarslan, J. Wilmers, Prog. Mater. Sci. 96 (2018) 322–384.
[29] B. Laurence, Homogenization of Elasto-(visco)plastic Composites: History-dependent Incremental and Variational Approaches, Institute Of Mechanics, Materials And Civil Engineering, Université catholique de Louvain, 2011.
[30] M.M.J. Treacy, T.W. Ebbesen, J.M. Gibson, Nature 381 (1996) 678–680.
[31] E.W. Wong, P.E. Sheehan, C.M. Lieber, Science 277 (1997) 1971–1975.
[32] M.F. Yu, O. Lourie, M.J. Dyer, K. Moloni, T.F. Kelly, R.S. Ruoff, Science 287 (2000) 637–640.
[33] A. Ghavamian, M. Rahmandoust, A. Öchsner, Comput. Mater. Sci. 62 (2012) 110–116.
[34] Y.I. Jhon, C. Kim, M. Seo, W.J. Cho, S. Lee, Y.M. Jhon, Sci. Rep. 6 (2016) 20324.
[35] V.N. Popov, V.E. Van Doren, Phys. Rev. B 61 (2000) 3078–3084.
[36] T. Tokunaga, K. Kaneko, Z. Horita, Mater. Sci. Eng. A 490 (2008) 300–304.
[37] J.B. Bunge, Texture Analysis in Materials Science: Mathematical Methods, Butterworths, London, 1982.
[38] H. Wang, B. Clausen, L. Capolungo, I.J. Beyerlein, J. Wang, C.N. Tome, Int. J. Plast. 79 (2016) 275–292.
[39] O. Muransky, P. Sittner, J. Zrnik, E.C. Oliver, Metall. Mater. Trans. A 39A (2008) 3097–3104.
[40] S.R. Agnew, R.P. Mulay, F.J. Polesak, C.A. Calhoun, J.J. Bhattacharyya, B. Clausen, Acta Mater. 61 (2013) 3769–3780.
[41] Z.Y. Liu, B.L. Xiao, W.G. Wang, Z.Y. Ma, Carbon 69 (2014) 264–274.
[42] J. Coër, P.Y. Manach, H. Laurent, M.C. Oliveira, L.F. Menezes, Mech. Res. Commun. 48 (2013) 1–7.
[43] A. Yilmaz,Sci. Technol. Adv. Mater. 12 (2011), 063001.
[44] M. Zhang, R. Li, J. Ding, H. Chen, J.S. Park, J. Almer, Y.D. Wang, Mater. Res. Lett. 6 (2018) 662–667.
[45] X. Feng, G. Fischer, R. Zielke, B. Svendsen, W. Tillmann, Mater. Sci. Eng. A 539 (2012) 205–210.
[46] C.Y. Yu, P.W. Kao, C.P. Chang, Acta Mater. 53 (2005) 4019–4028.
[47] B. Clausen, T. Lorentzen, T. Leffers, Acta Mater. 46 (1998) 3087–3098.
[48] M.R. Daymond, M.A.M. Bourke, R.B. VonDreele, B. Clausen, T. Lorentzen, J. Appl. Phys. 82 (1997) 1554–1562.
[49] G. Song, Z. Sun, L. Li, B. Clausen, S.Y. Zhang, Y. Gao, P.K. Liaw, Sci. Rep. 7 (2017) 45965.
[50] B. Clausen, T. Lorentzen, M.A.M. Bourke, M.R. Daymond, Mater. Sci. Eng. A 259 (1999) 17–24.
[51] S. Van Petegem, J. Wagner, T. Panzner, M.V. Upadhyay, T.T.T. Trang, H. Van Swygenhoven, Acta Mater. 105 (2016) 404–416.
[52] R. Fernandez, G. Bruno, G. Gonzalez-Doncel, Mater. Sci. Eng. A 403 (2005) 260–268.
[53] S. Roy, J. Gibmeier, V. Kostov, K.A. Weidenmann, A. Nagel, A. Wanner, Acta Mater. 59 (2011) 1424–1435.
[54] V.C. Nardone, K.M. Prewo, Scr. Metall. 20 (1986) 43–48.
[55] B. Chen, J. Shen, X. Ye, L. Jia, S. Li, J. Umeda, M. Takahashi, K. Kondoh, Acta Mater. 140 (2017) 317–325.
[56] H. Conrad, S. Feuerstein, L. Rice, Mater. Sci. Eng. 2 (1967) 157–168.
[57] T. Narutani, J. Takamura, Acta Metall. Mater. 39 (1991) 2037–2049.
[58] K.H. Chia, K. Jung, H. Conrad, Mater. Sci. Eng. A 409 (2005) 32–38.
[59] Z.C. Cordero, B.E. Knight, C.A. Schuh, Int. Mater. Rev. 61 (2016) 495–512.
[60] A. Lehtinen, L. Laurson, F. Granberg, K. Nordlund, M.J. Alava, Sci. Rep. 8 (2018) 6914.
[61] Z.Y. Zhong, H.G. Brokmeier, W.M. Gan, E. Maawad, B. Schwebke, N. Schell, Mater. Charact. 108 (2015) 124–131.
[62] G.I. Taylor, Proc. Royal Soc. Lon. Ser. A 145 (1934) 362–387.